Reliability Engineering and System Safety 275 (2026) 112675

Contents lists available at ScienceDirect

Reliability Engineering and System Safety

journal homepage: www.elsevier.com/locate/ress

Unification of multi-source and multi-fidelity fragility functions

Mohammad Amin Hariri-Ardebili [a,b,1,*], Siamak Sattar [b]

[a] University of Maryland, College Park, MD, USA
[b] National Institute of Standards and Technology, Gaithersburg, MD, USA

ARTICLE INFO

Keywords:
Fragility analysis
Uncertainty quantification
Optimization
Probabilistic simulations

ABSTRACT

The derivation of fragility functions through nonlinear dynamic analysis is a domain that has garnered significant attention historically. The majority of prior research efforts have been focused on the ground motion record-to-record variability and the incorporation of material randomness within numerical simulations. However, there remains an underexplored area concerning the uncertainties associated with the numerical modeling of structural physics. Diverse numerical models, ranging from low to high fidelity, necessitate varying degrees of material and modeling parameters, leading to disparate fragility outcomes. This divergence underscores the imperative need for methodologies that combine these varying functions into a cohesive framework for risk evaluation.

This paper introduces a framework that offers varied practical methodologies for the formulation of fragility functions, which encapsulate the triad of uncertainties: record-to-record variability in ground motion, material property randomness, and modeling strategy selections. Utilizing a case study of a reinforced concrete bridge pier, supplemented by shake table experimental results and the findings from a blind prediction contest, the study evaluates a suite of approaches for unifying multiple fragility functions obtained from different uncertainty sources and model fidelities. These approaches include decision tree selection, uniform/non-uniform weighting, mixed engineering demand parameter integration, and variance–bias decomposition to synthesize a unified fragility representation.The findings highlight the substantial variability in outcomes based on data accessibility, underlying assumptions in the combination process, and the fidelity of the employed models.

1. Introduction

The principle of demand versus capacity serves as a foundational element in the realm of structural engineering, guiding both design and analytical methodologies. Historically, this principle has been interpreted through a dichotomous lens, simplifying structural performance assessment into binary outcomes: either failure (represented as zero) or success (denoted by one). This binary framework, however, omits the range of intermediate performance between the two extreme (binary) states—i.e., acceptable performance ("success") and failure/collapse—prompting the introduction of the fragility concept [1].

In a broad definition, a fragility function articulates the probability of occurrence of an undesirable event as a function of an environmental stressor. Within the field of Earthquake Engineering, the stressor typically manifests as ground motion, leading to the widespread use of the term "seismic fragility" to denote the probability of specific damage levels occurring as a function of ground motion intensity. The inception of seismic fragility functions can be traced back to [2], who quantified component failure in a nuclear power plant as a function of peak ground acceleration (PGA). Substantial advancements in the conceptualization of seismic fragility occurred between 1980 and 2000. Ultimately, the Pacific Earthquake Engineering Research (PEER) center formally integrated the fragility concept into the Performance-Based Earthquake Engineering framework (PBEE) [3].

The conditional probability $\mathbb{P}[\text{EDP} \geq edp|\text{IM} = im]$ is typically called fragility or "demand fragility" [4], where EDP and IM refer to engineering demand parameter and intensity measure, respectively.

Several seminal contributions have advanced the research landscape on seismic fragility functions through diverse techniques and assumptions, as exemplified by [5–12]. A comparative analysis of various methodologies for constructing fragility functions has been extensively discussed in works such as [13–24]. In-depth reviews of the current state-of-the-art spanning various structural types can be found in comprehensive papers such as [25–27]. To keep the Introduction focused, we summarize the most relevant recent extensions and remaining gaps immediately below, and then

* Corresponding author.
E-mail address: amin.hariri@nist.gov (M.A. Hariri-Ardebili).
[1] (NIST PREP Researcher)

https://doi.org/10.1016/j.ress.2026.112675
Received 10 November 2025; Received in revised form 18 March 2026; Accepted 30 March 2026
Available online 4 April 2026

motivate the specific gap addressed herein: consistent propagation and integration of multiple uncertainty sources into a unified fragility representation.

Noteworthy reports addressing seismic fragility functions include the guideline developed by [28], offering comprehensive guidance for deriving fragility functions across buildings, lifelines, transportation networks, and critical facilities. An expanded version of this guideline was subsequently published as an edited book by [29]. The World Bank conducted a systematic review of diverse fragility models, as documented in [30]. The Encyclopedia of Earthquake Engineering [31] features multiple entries discussing fragility functions[32]. provides a historical review of the equations employed in developing fragility functions[33]. presents a comprehensive report on the fragility, vulnerability, and risk of engineering structures.

Beyond conventional fragility modeling, recent developments extend the framework and reduce epistemic and aleatory uncertainties through multivariate formulations, learning-based surrogates, time/state dependence, and rare-event simulation. In parallel, non-/semi-parametric fragility representations (e.g., kernel density estimation and Bayesian non-parametric models) have gained traction to reduce reliance on restrictive distributional assumptions and to better exploit data-driven fragility estimation [34]. Multivariate and multidimensional fragility functions (e.g., vector IMs and explicit dependence structures) have been investigated by [35,36]. Yan et al. [37] propose a hierarchical uncertainty-quantification framework for seismic fragility assessment. Physics-informed neural-network approaches to fragility have been proposed in [38], while deep-learning-assisted curve construction is explored in [39–41]. More generally, surrogate-model pipelines (including Gaussian processes, polynomial expansions, and tree-based learners) for efficient fragility estimation are benchmarked in [42–44]. Time-dependent fragility analyses are examined by [45], and a non-intrusive UQ-based framework for *state-dependent* fragility functions is introduced by [46]. Gauchy et al. [47] investigate uncertainty quantification and global sensitivity of fragility curves using Kriging-based surrogates[48]. present an adaptive algorithm integrated with standard fragility workflows to jointly account for aleatory and epistemic uncertainties. For networked systems, [49] develop a specialized subset-simulation scheme to evaluate network fragility curves in a single run. Site-independent fragility construction via spectrum-consistent transformation of spectral ordinates is presented by [50]. Spatiotemporal fragility models capturing dependencies between load indices and failure probability have also been proposed [51]. The implications of component damage correlation on system-level fragility are quantified by [52]. Collectively, these advances broaden applicability, improve efficiency, and sharpen interpretability of fragility-based risk assessments.

Although all previous studies provide valuable insights into the concept of fragility functions and their formulations, there still exists a gap in our comprehensive understanding of how different sources of uncertainties can be propagated within the fragility models and how they should be integrated into a unified model [53–56]. Uncertainty may originate from various sources, and there is not a single method to categorize them all [57,90]. In this paper, we adopt a practical approach to classify them into primary and secondary sources. The primary source includes ground motion, material, and modeling uncertainties, which are the focus of this paper. The secondary source encompasses decisions (which may not necessarily be sources of uncertainty) and includes the definition of limit state (LS) [58], choice of probabilistic analysis techniques [55], choice of IM parameter [59], and the choice of fragility function fitting method [17] that are not discussed in this paper, simply to keep the paper of manageable size for the readers and not because they are unimportant.

In this context, the main goal of this paper is to evaluate and compare practical methods for integrating fragility curves derived under different model fidelities, assumptions, and data sources into a unified fragility representation.

Traditionally, the analytical fragility functions[1] focus on ground motion record-to-record (RTR) variability quantification using probabilistic approaches.[2] This involves first building a numerical (often finite element) model of the engineering structure and then subjecting it to a large number of scaled or unscaled ground motion records. This is achieved by conducting a total of N_1 nonlinear transient simulations using a probabilistic analysis method (e.g., incremental dynamic analysis, multiple stripe analysis, and cloud analysis). Subsequently, a series of damage states (DS) are defined, as well as LSs (to separate DSs), and a form of fragility model is fitted to the discrete data points typically using an optimization algorithm (e.g., maximum likelihood). For example, the following analytical model is probably the most common form that uses a log-normal cumulative distribution function (CDF) to represent the probability of exceeding a particular EDP (i.e., edp) as a function of ground motion IM:

$$\mathbb{P}\left[\text{EDP} \geq edp|\text{IM} = im_i\right] = \Phi\left(\frac{\ln(im_i) - \ln(\eta)}{\beta}\right) \tag{1}$$

where $\Phi(.)$ is the standard normal CDF, β the logarithmic standard deviation (also called dispersion), and η median ($\ln \eta$ is mean) of the fragility function.

As long as a fixed/deterministic finite element model of the structure is used in probabilistic simulations, Eq. (1) represents only the uncertainty associated with the RTR variability. It is also relatively straightforward to incorporate uncertainties in the mechanical properties of materials, arising from limited knowledge about exact material properties (e.g., insufficient tests, time-dependent degradation, and deterioration) [62] into the fragility models. Often, a representative number of material properties can be sampled and used in finite element simulations. The sampling of material properties, their correlation, and combination is a separate line of research; however, for practical purposes, simple yet efficient methods such as Latin Hypercube Sampling can be adopted. Suppose a total of N_2 material samples (and thus representative finite element models) are identified to be sufficient. Those samples can be indirectly or directly combined with N_1 simulations with RTR variability, which may require a total simulation range from $\max(N_1, N_2)$ to $N_1 \times N_2$. Again, a similar post-processing as previously discussed can be conducted to derive a fragility function that incorporates both the ground motion RTR variability and the material property randomness [63,64].

A challenge may arise when various modeling strategies are available for a given structure, and there is a possibility that different analysts, or even a single analyst at different times, may adopt different strategies. For instance, modeling a reinforced concrete (RC) structure can be accomplished using a range of techniques from the equivalent single degree of freedom (SDOF) model, through the lumped plasticity model, to the distributed plasticity model. Each approach presents its own set of advantages and drawbacks. In certain cases, the validity of these model types depends on the extent of experimental tests available. Low-fidelity models may be more accurately calibrated with

[1] The majority of references, discussion, and case study examples in this paper are about seismic fragility. However, similar discussions can be expanded to other hazard sources too.

[2] Ground motion RTR variability is only one component of the uncertainty carried by the seismic input: the selection of the ground motion suite (including hazard-consistent conditioning and scaling) can materially influence both the estimated dispersion and the resulting fragility curves. Recent risk assessment frameworks therefore treat record selection and the handling of GMPE randomness as central steps in the overall uncertainty propagation and risk calculation (e.g., [60]). In addition, beyond RTR variability within a fixed suite, one may observe set-to-set variability and systematic bias across different “generic” or pre-collected suites, which can shift both the median and dispersion of fragilities even when the structural model is unchanged; see, e.g., [61]. These issues are particularly consequential when ground motion uncertainty interacts with material/modeling uncertainty, since the relative contribution of each source can depend on the chosen suite and selection protocol.

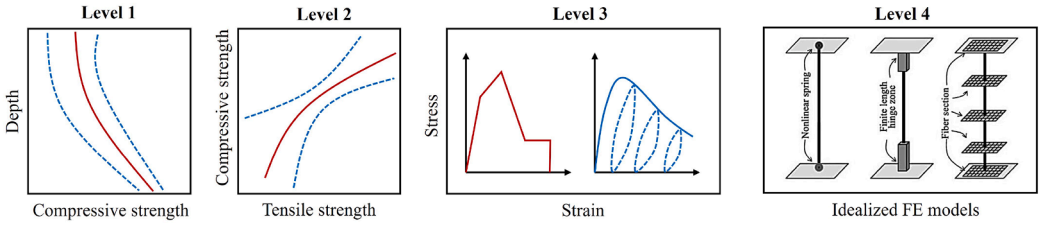

(a) Modeling uncertainty "slices" (classification), adapted from [75] with changes

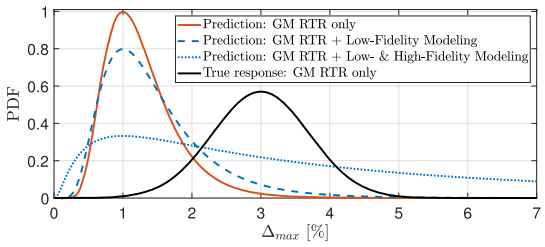

(b) Illustrative scenarios for combining modeling uncertainty (high-/low-fidelity) with RTR variability

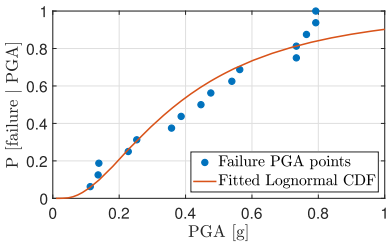

(c) Workshop-derived dispersion in estimated failure PGA, adapted from [79] with changes

Fig. 1. A set of illustrative topics related to modeling-type uncertainty quantification in fragility analysis.

limited data, whereas the presence of extensive data aids in the calibration process for high-fidelity models, which often include a larger number of unknown parameters. Additionally, a specific modeling strategy might be more suitable for either low or high loading intensities. For example, employing a distributed plasticity model is deemed appropriate for structures subjected to low-intensity seismic motions. Lastly, the choice of nonlinear mechanism modeling also hinges on the analyst's understanding and confidence in predicting the structure's behavior. For instance, if the location of potential cracks in a concrete structure is known, a discrete crack model is generally recommended; conversely, when the crack location is uncertain, a smeared crack model is favored.

This paper addresses three principal sources of uncertainty in reinforced concrete systems, with a particular focus on modeling uncertainty. It investigates how fragility functions derived under different modeling strategies, assumptions, and data sources can be integrated into a unified representation, and how the resulting unified fragility model varies as a function of the chosen integration assumptions. Several components of the proposed workflow rely on established concepts: (i) model-rating notions for comparing alternative model classes and fidelities, (ii) basic weighting/aggregation ideas, and (iii) the bias–variance viewpoint for interpreting prediction error. Other elements can be viewed as *extensions/adaptations* of prior work in the broader fragility/PBEE literature, including the use of mixed EDPs and bias/variance-type diagnostics, but here repurposed specifically for the unification of fragility curves across heterogeneous uncertainty sources and fidelity levels.

The new contribution of this paper is not the individual concepts (e.g., decision trees, weighting, or bias–variance decomposition per se), but a systematic, benchmarked comparison of multiple fragility-unification strategies applied to the same reinforced-concrete case study with consistent calibration and validation. Specifically, we introduce and/or formalize four unification families—(1) decision-tree selection, (2) uniform/non-uniform weighting, (3) mixed-EDP integration, and (4) variance–bias decomposition—and implement eight practical methodologies for combining fragility functions across multiple uncertainty sources and model fidelities. These methodologies are evaluated using calibrated numerical models with shake-table test validation; additionally, results from an international blind prediction contest are incorporated to quantify bias and variance in a manner that is external to the model-development process. Overall, the paper provides a comparative analysis of implementable fragility-integration approaches and clarifies the trade-offs they induce in unified fragility estimates and epistemic uncertainty.

Section 2 offers an overview of modeling uncertainty, its integration, and its significance relative to other commonly considered sources of uncertainty. Section 3 provides insights into the case study, the types of uncertainty sources considered, and the derivation of separate fragility functions, while Section 4 discusses different approaches to their unification.

2. Modeling uncertainty: An overview

This section provides a concise overview of modeling uncertainty, its classification, and its relevance to fragility analysis of reinforced concrete structures. Readers are assumed to be familiar with the other two primary sources of uncertainty—ground motion RTR variability [65–67] and material randomness [68–71]—or to seek additional background elsewhere.

In seismic analysis, modeling uncertainty reflects the limitations of an idealized numerical representation in capturing real structural behavior under earthquake loading. Its definition is not uniform; for example, [72] describe it as *"the variability of the physical properties and behavior of a structure for a given design realization."* [73] similarly emphasize the variability associated with a model's ability to represent the true response. Building on [74,75], Fig. 1(a) summarizes four "slices" of modeling uncertainty:

Level 1. Uncertainty in measured physical properties (e.g., concrete tensile strength, soil stiffness), which does not alter the numerical formulation but affects simulation inputs.

Level 2. Uncertainty in mapping measured properties to constitutive-model parameters (e.g., strength measures versus parameters required by a chosen law) [76,77], closely related to material randomness.

Level 3. Uncertainty in selecting the constitutive model and associated simplifying assumptions [78] (e.g., plasticity/damage/fracture-type formulations for concrete).

Level 4. Uncertainty in the overall modeling approach (e.g., lumped versus distributed plasticity, treatment of interaction mechanisms, boundary conditions, and damping), including fidelity-related modeling decisions.

Fig. 1(b) further illustrates how uncertainty sources can be combined at different fidelity levels [75]. Relative to a deterministic model with

only RTR variability, incorporating low-fidelity modeling uncertainty (Levels 1–2) increases dispersion modestly, whereas introducing high-fidelity modeling uncertainty (typically associated with constitutive-model and parameter choices) can increase dispersion more substantially. This distinction is closely tied to the dimensionality of the uncertain-parameter space: low-fidelity models typically involve fewer uncertain inputs, while higher-fidelity models require a broader set of parameters.

An additional illustration of modeling-type uncertainty is provided by [79], which synthesizes an international benchmark study in which participants analyzed the same structure under prescribed geometry, loading protocol, damping, material properties, and input motions, but were free to choose their modeling and solution strategies. Differences in the discretization of the finite element model, time integration methods, mesh type and size, convergence criteria, formulations and boundary conditions for soil-structure and water-structure interactions, constitutive assumptions, and the type of damage led to substantial variability in inferred failure thresholds [79,80]; for the same system, estimated failure PGA values spanned 0.1–0.8g (Fig. 1(c)). The fitted lognormal model yielded a logarithmic standard deviation of approximately 0.7, exceeding typical values reported for RTR variability (often around 0.4), underscoring the influence of modeling choices on response uncertainty.

To bridge the general uncertainty taxonomy in Section 2 and the implementation details in Section 3, we briefly summarize the modeling/material-uncertainty propagation framework introduced in [71] in Algorithm 1. This condensed workflow is provided primarily to define the model families and uncertainty pools used in the case study and to establish the inputs required for the subsequent fragility unification strategies developed in this paper.

Algorithm 1 Workflow for modeling/material uncertainty propagation as input for the multi-model integration

Require: Physical data for a target RC component/system (e.g., member, subassembly, building, or infrastructure); parent-model set $\mathcal{M} = \{M^{(1)}, \ldots, M^{(N_p)}\}$; modeling-variable pool $\mathcal{X}_m$; material-variable pool $\mathcal{X}_u$; analysis protocol (e.g., IDA/MSA/Cloud); limit states $\{\mathrm{LS}_k\}$; intensity measure IM; demand measures $\{\mathrm{EDP}_\ell\}$.

1: **Define parent models (model-class uncertainty).** Select fundamentally different, scientifically defensible modeling strategies for the same RC component/system (e.g., lumped-plasticity vs distributed-plasticity/fiber-based vs spring/hinge-zone variants), forming $\mathcal{M}$.

2: **Define uncertainty pools and their mapping to the RC component/system.**

(a) *Modeling (Type-I) variables* $\mathcal{X}_m$: N_{gip} (Gauss integration points in force-based fiber elements), N_{elem} (number of elements in displacement-based fiber models), ξ_{cr} (damping ratio), ξ_{type} (damping formulation: Rayleigh constant/updating vs modal), $\mathrm{Geo}_{\mathrm{type}}$ (geometric transformation: corotational / P–Δ / linear), M_{dsct} (mass discretization: lumped vs distributed), $\mathrm{CS}_{\mathrm{dsct}}$ (cross-section discretization / fine vs coarse), $\mathrm{Conc}_{\mathrm{type}}$ (concrete constitutive-model choice), $\mathrm{Stl}_{\mathrm{type}}$ (steel constitutive-model choice), $\mathrm{Conc}_{\mathrm{rgz}}$ (concrete regularization on/off), $\mathrm{Stl}_{\mathrm{rgz}}$ (steel regularization on/off), I_C (effective inertia / stiffness selection for simplified models), λ (cyclic deterioration rule/parameterization), $\mathrm{LMF}_{\mathrm{type}}$ (lumped-plasticity formulation option), L_P (plastic-hinge length / plastic-zone ratio), L_i (initial fiber length beneath hinge-zone variants).

(b) *Material (Type-II) variables* $\mathcal{X}_u$: f_{ym} (steel yield stress), f_u (steel ultimate stress), ε_f (steel fracture strain), E_s (steel elastic modulus), b (steel strain-hardening ratio), E_{c0} (unconfined concrete elastic modulus), f_{c0} (unconfined concrete compressive strength), ε_{c0} (unconfined concrete peak strain), f_t (concrete tensile strength), E_{cc} (confined concrete elastic modulus), f_{cc} (confined concrete compressive strength), ε_{cc} (confined concrete peak strain), E_{ccdeg} (concrete softening modulus / post-peak degradation slope).

3: **Generate Type-I children models (modeling-parameter uncertainty within each parent).** For each parent $M^{(p)} \in \mathcal{M}$, identify the applicable subset $\mathcal{X}_m^{(p)} \subseteq \mathcal{X}_m$ and generate a design-of-experiments – DOE (e.g., randomized complete block design) over categorical/choice variables to obtain $\{M_{m,i}^{(p)}\}_{i=1}^{N_m^{(p)}}$.

4: **Generate Type-II children models (material randomness within each parent).** For each parent $M^{(p)} \in \mathcal{M}$, identify the applicable subset $\mathcal{X}_u^{(p)} \subseteq \mathcal{X}_u$ and draw correlated realizations using LHS/MCS to obtain $\{M_{u,j}^{(p)}\}_{j=1}^{N_u^{(p)}}$.

5: **Generate grandchildren models (combined modeling–material uncertainty).** Construct combined realizations $\{M_{(m,u),k}^{(p)}\}$ by pairing Type-I and Type-II children models (direct pairing for full factorial coverage or randomized pairing for reduced cost), yielding $N_{mu}^{(p)}$ combined models.

6: **Nonlinear dynamic analyses.** Analyze all models under the chosen excitation protocol and extract demand histories $\mathrm{EDP}_\ell(\mathrm{IM})$ and limit-state exceedance indicators $\mathbf{1}[\mathrm{LS}_\mathbf{k}]$.

7: **Within-parent fragility estimation (separate by uncertainty source).** For each parent $M^{(p)}$, estimate: (i) fragilities from $\{M_{m,i}^{(p)}\}$ (modeling-only), (ii) fragilities from $\{M_{u,j}^{(p)}\}$ (material-only), and (iii) fragilities from $\{M_{(m,u),k}^{(p)}\}$ (combined). Store parameters $(\hat{\theta}, \hat{\beta})$ and goodness-of-fit diagnostics for each case.

8: **Outputs for integration/unification across sources and fidelities.** Collect the set of candidate fragility curves $\{\mathcal{F}_s^{(p)}\}$ across parents and uncertainty categories ($s \in \{m, u, mu\}$) as the input ensemble for the paper's unification strategies (selection/weighting/mixed-EDP/bias–variance-based synthesis).

3. Description of the case study

For the purpose of unifying fragility function models, this paper utilizes a well-known bridge pier example, the 2010 UCSD shake table test featuring a reinforced concrete column [81]. Probabilistic simulations with various uncertainties have been previously detailed in two other papers [71,82] and will not be reiterated here. The column is circular, with a diameter of 1.22 m and a height of 7.32 m, inclusive of a footing for attachment to the shake table, See Fig. 2(a). Additionally, a large concrete block atop the column (representative of the superstructure) carries a weight of 2.32 MN.

3.1. Uncertainty sources and scenarios

Three primary sources of uncertainties (i.e., ground motion RTR variability, material randomness, and modeling uncertainty) are applied to this example. Modeling uncertainty is addressed by developing three parent models employing different numerical strategies: a Lumped Plasticity model (LuP) concentrating nonlinearity solely at the column's base; a Distributed Plasticity model (DiP) applying nonlinearity across the entire column length; and a Finite-Length Hinge Zone model (FLHZ), positioned between the previous two, applying nonlinearity only to a limited portion of the column. Detailed discussions on this are available in [71]. All these three parent models (i.e., DiP, FLHZ, and LuP) are first calibrated with experimental results in terms of drift ratio. For example, Fig. 2(b) illustrates the results of best DiP model against recorded drift ratio from six ground motions used in shake table test.

Material uncertainty is managed by assuming an appropriate distributional model, including mean, standard deviation, and correlation for 13 properties in confined and unconfined concrete, as well as longitudinal rebars. Extensive details are provided in [82]. Finally, ground motion RTR variability is incorporated using the multiple stripe analysis (MSA) method at nine intensity levels, with 40 scaled ground motions in each.

For the purposes of this study, we consider four probabilistic simulation scenarios that progressively activate the main uncertainty sources

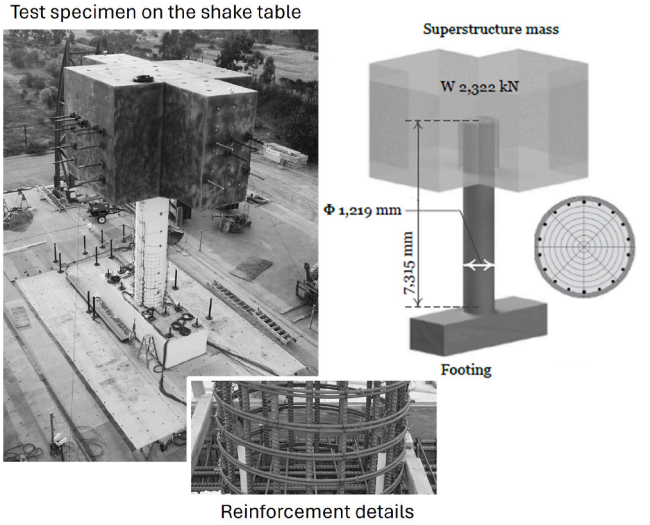

(a) Experimental specimen and numerical model; photo adopted from [81]

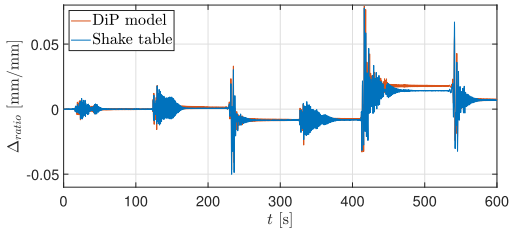

(b) A sample of calibration of numerical model

Fig. 2. Case study RC bridge pier including the shake table test and calibrate model.

discussed in Section 2. The intent is to (i) isolate the marginal effect of each source (RTR, material, modeling) on the resulting fragility functions, and (ii) generate consistent ensembles of fragility curves that can be subsequently integrated using the unification strategies proposed in this paper. The modeling- and material-uncertainty pools, and the corresponding sampling/assembly logic (children and grandchildren model families), are summarized in Algorithm 1; additional implementation details and variable-selection rationale are provided in our companion study. The scenarios are defined as follows:

Scenario GM: Fragility functions are derived by accounting only for ground-motion RTR variability while using a deterministic numerical model (fixed material and modeling parameters).

Scenario GMAT: Fragility functions are derived by combining ground motion RTR variability with material property randomness. Material realizations are generated by Latin Hypercube Sampling (LHS) of the concrete/steel properties listed in Algorithm 1 (with the adopted correlation assumptions), and each realization is analyzed under the selected ground motion suite.

Scenario GMOD: Fragility functions are derived by combining ground motion RTR variability with modeling-type variability. Modeling realizations are generated via a structured design-of-experiments over the discrete/categorical modeling choices listed in Algorithm 1 (e.g., discretization, damping model, constitutive model options). These "children" modeling configurations are then propagated through nonlinear dynamic analyses under the selected ground motion suite.

Scenario GMM: Fragility functions are derived by combining all three sources of uncertainty. Specifically, for each parent modeling strategy, Type-I (modeling) and Type-II (material) realizations are paired to form combined model instances ("grandchildren" models in Algorithm 1), which are then analyzed under the selected ground motion suite.

3.2. Modeling/Material uncertainty integrated in fragility functions

The outcome of probabilistic seismic simulation is best presented in the form of fragility functions. A lognormal distribution is fitted to discrete data points using the maximum likelihood method (MLE) as proposed in [9]:

$$\{\hat{\theta},\hat{\beta}\} = \underset{\hat{\theta},\hat{\beta}}{\text{argmax}} \sum_{i=1}^{N} \left[\ln\binom{N_i^t}{N_i^f} + N_i^f \ln\left(\Phi\left(\frac{\ln(im_i)-\ln(\theta)}{\beta}\right)\right) + (N_i^t - N_i^f)\ln\left(1-\Phi\left(\frac{\ln(im_i)-\ln(\theta)}{\beta}\right)\right)\right] \quad (2)$$

where N_i^f and N_i^t are number of failed and total data points at seismic intensity level IM = im_i, N is the number of seismic intensity levels (SILs); $\hat{\theta}$ and $\hat{\beta}$ are the estimated median and logarithmic standard deviation, respectively.

Fig. 3 presents fragility functions in terms of $\hat{\eta}$ and $\hat{\beta}$ for four uncertainty scenarios (i.e., GM, GMOD, GMAT, and GMM), three parent models (i.e., LuP, FLHZ, and DiP), and a continuous range of limit states from 0 to 8% drift ratios. The variation among the fragility curves due to ground motion RTR uncertainty alone (GM scenario) is minimal, stemming from fundamental assumptions in developing the parent models. Converting physics-based material properties used in distributed plasticity models to parameters in phenomenological lumped plasticity models introduces another layer of uncertainty. As the limit state value increases, the dispersion among the curves, both in median and standard deviation, also increases. Incorporating material uncertainty (GMAT) has only a minor effect on the fragility functions. In contrast, modeling uncertainty (GMOD) leads to significant variation in fragility functions. GMM scenario closely resembles GMOD, indicating that the major source of uncertainty arises from modeling-related parameters. Comparing the $\hat{\eta}$ and $\hat{\beta}$ values reveals a high correlation between GM with GMAT and GMOD with GMM. The variability among the fragility functions escalates with increasing LS values.

4. Results: Unification of fragility functions

In Section 3.2, fragility functions were generated for different parent models (i.e., various FE modeling techniques). However, the physical model of this structure has only one "true" (unknown) fragility function, regardless of the modeling technique used by the analyst. Therefore, it is crucial to combine the fragility functions developed with different parent models. This section will present various techniques to unify the fragility functions, discussed in Eq. (1).

Since the focus of this paper is solely on analytical fragility functions, it's important to understand the factors affecting the reliability of these functions before combining them. The quality, robustness, and reliability of the fragility functions depend on the following main factors [83]:

- Type of the intensity measure parameter (e.g., $S_a(T_1)$ or PGA).
- Damage characterization, including the damage model (i.e., damage index), damage indicators, and the number of damage states.
- Class definition (i.e., type of the system or component), sample size (i.e., single vs. multiple buildings, or randomization of parameters), and the sampling technique (e.g., crude Monte Carlo Simulation (MCS) vs. Latin Hypercube Sampling, or any design of experiment).
- Data quality, referring to analysis type (e.g., nonlinear static vs. dynamic method), degree of sophistication in the mathematical model (completeness of model, detailed material properties, high-fidelity configuration, and geometry), and the type of seismic demand (ground motion time history vs. code-based response spectra).
- Derivation of fragility functions, including the treatment and quantification of various sources of uncertainty, and the selection of fitting methods.

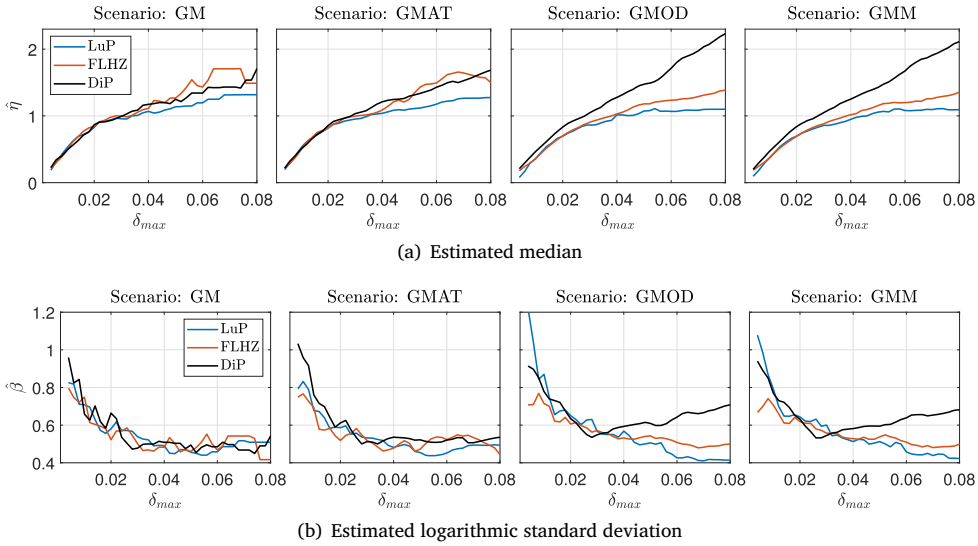

(a) Estimated median

(b) Estimated logarithmic standard deviation

Fig. 3. General comparison of fragility function parameters ($\hat{\eta}$ and $\hat{\beta}$) across uncertainty scenarios and parent models.

4.1. Decision-tree approach

To select the appropriate fragility function from a set of candidates, a method is needed. Rossetto et al. [83] proposed a rating framework that assesses the relevance and overall quality of fragility functions. Relevance is primarily based on the representativeness of the functions, while overall quality considers input quality, rationality, and documentation quality related to fragility functions. Once all candidate fragility functions are collected, the mean probability of collapse (C) for each level of seismic intensity is estimated from the sum of the weighted curves for the corresponding intensity measure level:

$$\mathbb{E}[\mathbb{P}[\mathrm{C}|\mathrm{IM}=im]]=\sum_{k=1}^{N_{\mathrm{ff}}} w_k \mathbb{P}\left[\mathrm{C}|\mathrm{IM}=im_k\right] \tag{3}$$

where N_{ff} is the number of fragility functions, and w_k is the associated uniform weights, which is computed using one three schemes as discussed below:

- The first weighting scheme (WS1) assigns equal weights to all functions, i.e., $w_k=\frac{1}{N_{\mathrm{ff}}}$. Epistemic uncertainty, arising from the presence of different models, is further quantified by fitting a beta distribution to the values of the fragility functions at each intensity level. This approach does not require that all fragility functions follow the same parametric model, e.g., the log-normal CDF.
- The second weighting scheme (WS2) is based on rating seven criteria corresponding to the overall quality of fragility functions. These criteria are: c_1- structural characteristics, c_2- seismic demand, c_3- choice of EDP, c_4- completeness of model, c_5- treatment of uncertainty, c_6- first principles, and c_7- documentation quality. Depending on how well they have been considered in a fragility function, they take a rating score of 1 (Low), 2 (Medium), and 3 (High). The sum of all these seven rating scores is then normalized such that the total sum of the weights for all fragility functions adds up to one.

$$w_k=\frac{\sum_{j=1}^{7} c_{j,k}}{\sum_{k=1}^{N_{\mathrm{ff}}}\sum_{j=1}^{7} c_{j,k}} \tag{4}$$

- The third weighting scheme (WS3) is based on user-defined weights, $w_k\in[0,1]$, for each fragility function. The user considers their relative confidence in the reliability and representativeness of each fragility function. The sum of the weights across all fragility functions must equal one.

Fig. 4 illustrates the combination of fragility functions using the decision tree approach. Fig. 4(a) and 4(b) use the three parent-model MLE fragility functions (LuP, FLHZ, and DiP) at two representative limit states. The *individual* curves correspond to these parent-model fragilities, whereas the colored curves represent their weighted combinations under the selected weighting schemes. In particular, WS1 assigns equal weights of 1/3 to each parent model, while WS3 assigns weights of 1/4 to LuP and FLHZ and 1/2 to DiP, reflecting its higher level of modeling sophistication. The resulting combined curves therefore differ, with the magnitude of the difference depending on the chosen limit state. Epistemic uncertainty associated with the combined curve is quantified using a beta distribution; its Probability distribution function (PDF) is shown at three $S_a(T_1)$ levels (1.0, 1.5, and 2.0 g).

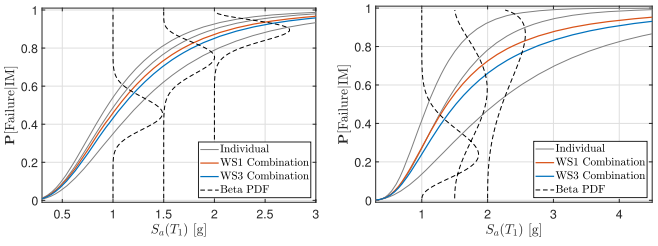

(a) LS = 0.04; MLE

(b) LS = 0.08; MLE

Fig. 4. Combining fragility functions using decision tree approaches in Section 4.1; all functions are based on GMM scenario.

4.2. Nonuniform weight function approach

The weight factors used in Eq. (3) are scalar values (i.e., uniform weight factors). This means they are independent of the IM level, and the same weight factor is assigned to a fragility function in its entire domain. This is a so-called uniform fragility functions combination. In contrast, a non-uniform weight scheme can be used where the weight factor is a function of the IM level, i.e., $w_k(im)$. This requires some physics-based information about the performance of each parent model under various seismic intensity levels. For example, it is known that the DiP models outperform the LuP models at lower intensity levels. On the other hand, the phenomenological LuP models are more reliable for larger deformations (i.e., post-capping) and the near-collapse region [77]. Therefore, an IM-dependent weight function seems more reasonable to combine

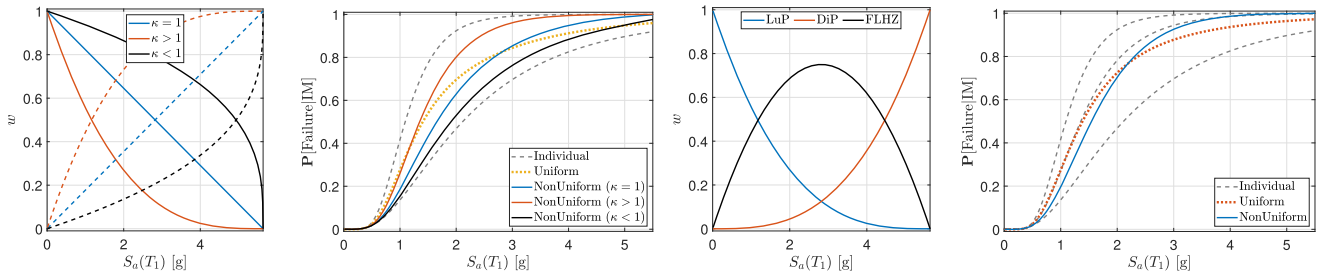

(a) Nonuniform weights for double combination

(b) Combined fragility functions

(c) Nonuniform weights for triple combination

(d) Combined fragility functions

Fig. 5. Combining fragility functions using non-uniform weight functions; all functions are based on GMM scenario; LS = 0.08; MLE

the fragility functions. To combine two fragility functions, a generic IM-dependent weight function can be defined as:

$$w_1(im) = \left(\frac{\mathrm{IM}_{max} - im}{\mathrm{IM}_{max} - \mathrm{IM}_{min}}\right)^{\kappa}; \quad w_2 = 1 - w_1 \tag{5}$$

where $\mathrm{IM}_{\min}$ and $\mathrm{IM}_{\max}$ are the lower and upper bound IM values (typically are chosen based on all LS values), and κ is exponent related to the rate of change in weight function at different IM levels.

Fig. 5(a) illustrates three intensity-dependent w_1 functions (solid lines) and their counterpart w_2 functions (dashed lines) for $\kappa = 1/3$, $\kappa = 1$, and $\kappa = 3$. These weights are then applied to two parent-model fragility functions (DiP and LuP) to construct unified fragility curves. In all cases, w_1 is assigned to DiP (i.e., relatively larger weights at lower intensity levels), and w_2 is assigned to LuP such that $w_1(\mathrm{IM}) + w_2(\mathrm{IM}) = 1$ for all IM. Fig. 5(b) shows the resulting nonuniform weighted summation, and compares it to the uniform combination (dashed yellow line) with $w = 1/2$ for each curve.

Fig. 5(b) also shows the strong influence of exponent κ in final fragility curve. Because κ is a tuning parameter rather than a universal material constant, we recommend selecting it *a priori* using one of the following pragmatic criteria: (i) adopt $\kappa = 1$ as a neutral baseline and treat $\kappa \in [1/3, 3]$ as a sensitivity band; (ii) when calibration/validation data are available, choose κ by minimizing a misfit metric between measured and predicted responses (or between experimentally-informed and unified fragilities); or (iii) specify a target weight at a reference intensity level (e.g., at a design IM) and solve for κ such that the desired transition behavior is satisfied. In this study, we report results for representative κ values to illustrate the sensitivity and avoid over-interpreting a single tuned choice.

The same concept extends directly to more than two fragility functions, with the only requirement that the weights remain non-negative and sum to one at each IM level, i.e., $\sum_{i=1}^{N_p} w_i(\mathrm{IM}) = 1$. Fig. 5(c) provides an illustrative set of three weight functions for the three parent models considered here: LuP receives larger weights at higher intensity levels, DiP dominates at lower intensities, and FLHZ primarily covers the intermediate range (consistent with its hybrid characteristics between concentrated and distributed plasticity representations). The resulting three-curve nonuniform combination is shown in Fig. 5(d) and compared against the equally-weighted uniform combination. Finally, we note that both uniform and nonuniform weighted combinations can introduce slight non-smoothness in the resulting unified fragility curve, particularly when parent-model fragilities differ markedly. Importantly, because $w_i(\mathrm{im}) \geq 0$ and $\sum_i w_i(\mathrm{im}) = 1$, the weighted combination preserves non-decreasing behavior provided the parent-model fragilities are non-decreasing; the lack of smoothness manifests mainly as kinks rather than decreasing segments.

4.3. Mixed-EDPs approach

In Section 4.2, we combined the fragility functions with non-uniform weights based on a justification that a particular parent model may provide a more accurate response for a certain range of seismic intensity. A similar idea can be used to mix the EDPs from different parent models before generating the fragility functions. This section provides various alternatives to combine the raw EDPs from different parent models towards generating fragility functions. This section presents the results in threefold: (1) multi-fidelity mixture (i.e., weighted mixing of all EDPs), (2) IM-dependent mixed-EDPs, and (3) sensitivity of fragility functions to seismic intensity levels.

A prerequisite for meaningful mixed-EDP integration is that the pooled EDP samples correspond to a compatible failure mechanism for the target limit state. When parent models emphasize different dominant mechanisms (e.g., flexural versus shear-controlled response in RC columns), mixing a single EDP across incompatible modes can obscure mode-specific limit states and lead to misleading fragility interpretations. Therefore, for general applications (particularly system-level analyses), we recommend partitioning the simulation outcomes into mode-consistent subsets and performing mixed-EDP integration within each subset (e.g., flexure, flexure–shear, and shear), followed by optional mode-combination using total probability when a global failure definition is needed. In practice, the partition may be conducted using a deterministic or probabilistic mode indicator based on capacity comparisons (or demand-to-capacity ratios) [84]. In the present study, the benchmark component is intentionally selected and modeled such that the governing limit states are drift-based and interpreted under a consistent component-level failure mechanism across the considered parent models; hence, explicit mode-partitioning is not exercised here.

4.3.1. Multi-fidelity mixed-EDPs

The goal of the mixed-EDP approach is to combine simulation outputs at the EDP-sample level prior to any fragility post-processing. At each SIL, we pool the raw EDP realizations generated by the parent models and then estimate the exceedance probabilities (or empirical CDFs) and the corresponding fragility functions from this mixed sample. Fig. 6 illustrates this concept for the GM scenario: at each SIL, each parent model contributes the same number of EDP samples (here, one EDP per ground motion), so the mixed-EDP sample is a simple concatenation of the three parent-model samples (e.g., 40 samples per parent model, yielding 120 mixed samples).

For simplicity, this section is limited to the GM scenario only; the same exercise was not repeated herein for the GMOD, GMAT, and GMM scenarios. For GMOD, GMAT, and GMM scenarios, the number of EDP samples contributed by each parent model may differ substantially because the number of children/grandchildren models and/or the sampling plans are not identical across parents. In such cases, a naive concatenation would implicitly assign larger weight to the parent model

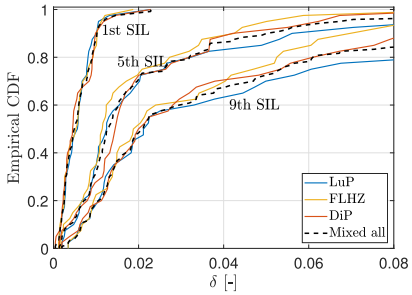

Fig. 6. Variation of EDP in parent models and the mixed version at three SILs. Results are shown for GM uncertainty scenario.

that happens to have more samples, which is generally not desirable. To avoid this artifact, we propose two technically consistent pooling strategies.

Strategy A (equal-parent contribution via balanced resampling). At each SIL and for each parent model $i \in \{1, \dots, N_p\}$, let $\{\text{EDP}_{i,n}\}_{n=1}^{N_i}$ denote the available samples, where N_i may differ across parents. Define a balanced mixed-EDP sample by drawing

$$N^\star = \min_i N_i \tag{6}$$

samples from each parent model (without replacement if $N_i = N^\star$, or with replacement if $N_i > N^\star$ is not to be downsampled), and then pooling the resulting $N_p N^\star$ samples. This produces an empirical CDF (and fragility estimate) in which each parent model contributes equally at that SIL, independent of the internal DOE size. To reduce Monte Carlo noise induced by resampling, the balanced pooling can be repeated B times (bootstrap-style) and the resulting mixed-EDP fragility statistics can be reported as the mean/interval across resamples.

Strategy B (explicitly weighted pooling). Alternatively, define intensity-dependent (or intensity-independent) parent-model weights $\{w_i(im)\}$ satisfying $w_i(im) \geq 0$ and $\sum_{i=1}^{N_p} w_i(im) = 1$. Then construct a weighted empirical CDF at each SIL by assigning each EDP sample from parent i the weight

$$\omega_{i,n}(im) = \frac{w_i(im)}{N_i}, \qquad n = 1, \dots, N_i, \tag{7}$$

so that the total probability mass contributed by parent model i is exactly $w_i(im)$, regardless of N_i. The resulting weighted empirical CDF (or weighted exceedance probability at each SIL) can then be used directly for fragility estimation. In the absence of additional information, one may adopt $w_i = 1/N_p$ (equal-parent weighting); when a model-rating, calibration score, or external benchmark is available, $w_i(im)$ can be selected to reflect relative credibility as a function of IM.

4.3.2. IM-dependent mixed-EDPs

The goal of the IM-dependent mixed-EDPs approach is to combine stripes from different parent models to generate a single fragility function [85]. In general, it is assumed that the fragility function is developed using N_{IM} stripes. The EDP results in each stripe come from a different parent model. If only two parent models (e.g., LuP and DiP) are used, then $K = 2$, and for the case with three parent models (LuP, FLHZ, and DiP), $K = 3$. The general solution for the number of all possible combinations is $\binom{N}{K}$. However, not all these combinations are reasonable from an engineering point of view. Following the discussion in Section 4.2, the distributed plasticity models are typically used for low-intensity stripes, while the lumped plasticity models are more appropriate for the collapse region. Therefore, a condition is added to the problem: for the stripes with increasing intensity, LuP should always appear after DiP (for two-model combinations), and LuP > FLHZ > DiP (for three-model combinations).

In the context of combinatorial mathematics, this problem falls under the category of the so-called star-and-bar (or balls-and-bars) method,

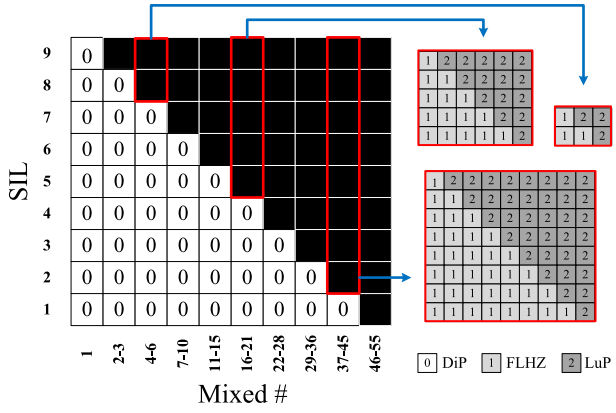

Fig. 7. Mixing EDPs from different parent models using star-and-bar combinational theorem. Model involves $N = 9$ stripes, and $K = 3$ parent models should be appear in a certain order (LuP > FLHZ > DiP).

which is a graphical aid for deriving certain combinatorial theorems [86]. In its most general form, for any pair of positive integers N and K, the number of K-tuples of non-negative integers whose sum is N is equal to the number of multisets of cardinality $K - 1$ taken from a set of size $N + 1$. This problem can be represented by a binomial coefficient. The number of mixed-EDP cases is:

$$N_{\text{Mixed-EDPs}} = \binom{N + K - 1}{K - 1} \tag{8}$$

This procedure is schematically illustrated in Fig. 7 for $N = 9$ stripes, and $K = 3$ parent models (LuP, FLHZ and DiP). Following Eq. (8), this yields to a total of 55 mixed combinations. Note that with only two parent models, a total of 10 mixed models are obtained.

Fig. 8 displays the MLE-based fragility functions for three limit states using two-model and three-model mixed-EDP combinations. In this case study, the mixing scheme in Fig. 8 is applied at the *stripe* level: at each SIL, one parent model is selected (according to the selected two-model or three-model combination rule) and its raw EDP sample for that stripe is used in the mixed dataset. The mixed-EDP dataset is then formed by concatenating the selected stripe-wise samples across all SILs and subsequently fitting the fragility by MLE.

For lower limit-state values, the parent-model fragilities are close, and therefore the mixed-EDP curves are nearly indistinguishable from the individual parent models. For LS = 0.08, however, the mixed-EDP fragility curves tend to align closely with the LuP model. This behavior is explained by the disproportionate influence of the highest stripe (SIL 9) on the MLE fit at this high limit state: exceedances (or near-exceedances) at the largest intensity levels strongly govern the inferred median and dispersion. In the three-model combinations, 45 out of 55 mixed realizations select LuP in the last stripe (in the two-model combinations, this is 10 out of 11 cases), so the mixed dataset is frequently "anchored" by the LuP response at SIL 9, which shifts the unified curve toward LuP. Finally, we note that in some instances stripe-wise mixing can yield exceedance rates that are locally higher than those of any single parent model at a given SIL; this is a consequence of pooling across heterogeneous parent-model response distributions and is not precluded by the mixed-EDP construction.

4.3.3. Sensitivity to IM level

Ideally, a fragility function can be developed using as few as two SILs (since it provides at least two points for curve fitting). Increasing the number of SILs improves the initial data points and enhances the quality of the fitted function. The distribution of initial data points also plays a crucial role in the fragility curve's quality. Selecting SILs to cover the major part of the fragility function improves accuracy and reduces uncertainty in the fitting process. This section explores the feasibility of using fewer SILs to regenerate fragility functions.

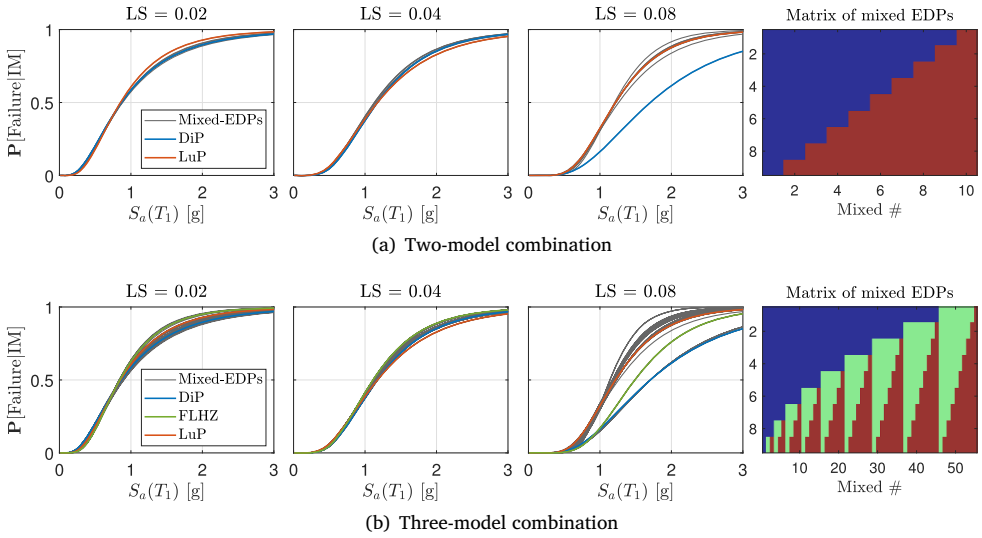

(a) Two-model combination

(b) Three-model combination

Fig. 8. Mixed-EDP-based fragility functions; all functions are based on GM scenario; three LSs are shown; MLE; the most right plot illustrates the matrix of mixed EDPs.

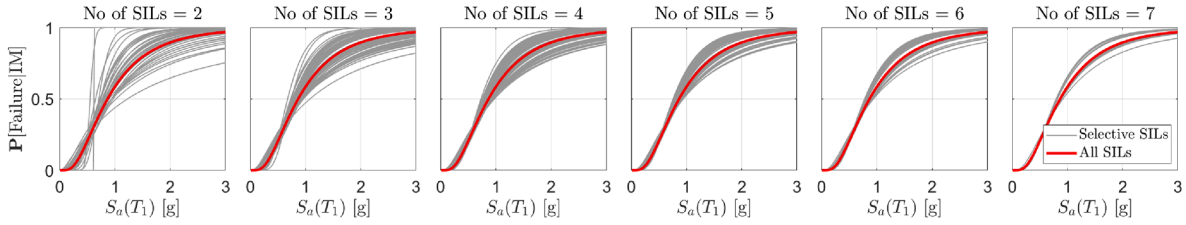

Fig. 9. Fragility functions regenerated from limited number of SILs with random selection (gray curves) including the deterministic case with all SILs (red curve); Only LS = 0.02 is shown for DiP model and GM uncertainty scenario with MLE. Number of random functions in each sub-plot is different.

Given an initial number of N seismic intensity levels, the total number of fragility functions that can be regenerated using K SILs is $\binom{N}{K}$. Considering all possible combinations, the total number of regenerated fragility functions is:

$$N_{\text{Fragility}} = \binom{N}{2} + \binom{N}{3} + \cdots + \binom{N}{N-1} \tag{9}$$

Since there are $N = 9$ initial SILs in our analyses, a total of 36, 84, 126, 126, 84, 36, and 9 new fragility functions can be regenerated based on two-layer to eight-layer SILs. This yields 501 new fragility functions for each of three parent models and four LS values. Fig. 9 illustrates regenerated fragility functions obtained using different numbers (and subsets) of SILs. The plot shows results for the DiP parent model under the GM uncertainty scenario at LS = 0.02, with all curves estimated via MLE under the assumed lognormal fragility form. In each panel, the reference (deterministic) fragility function based on all nine SILs is also shown (red curve). As expected, using more SILs generally improves the stability of the estimated fragility parameters and yields curves closer to the nine-SIL reference. Conversely, subsets with very few SILs—particularly two-SIL fits—can be unstable and produce poor estimates; therefore, these cases are included primarily as a sensitivity/robustness check to highlight data-sufficiency effects, not as a recommended minimal design.

Fig. 10 extends and summarizes the results (in terms of $\hat{\eta}$ and $\hat{\beta}$) for three parent models and two LS values. In each combinational level (i.e., combination of K SILs), the results are summarized to the median and standard deviation in the form of bar plots. Also, each figure includes a horizontal line that shows the deterministic model. Ideally, the statistics (i.e., $\hat{\eta}$ and $\hat{\beta}$) from regenerated fragility functions should yield the value obtained from the deterministic model. Any change presents the bias and variance of the newly generated functions. In general, the variation in $\hat{\beta}$ is less than $\hat{\eta}$. This shows that the regenerated fragility functions are mostly shifted than rotated. For the current example, using $K = 4$ or more SILs provides good results, while using $K = 2$ is not recommended. In general, the estimated results for LS = 0.02 are better than LS = 0.08 because the lower limit state covers a larger part of the fragility function. All three parent models illustrate a similar trend; however, the quality of regenerated plots seems a bit better for LuP model.

The discussion so far has focused on the overall quality of the regenerated fragility functions, summarizing their mean and standard deviation for any K number. However, such a discussion doesn't provide information about the quality of individual SIL combinations in regenerating fragility functions. Figs. 11 and 12 address this issue. To compare the results of hundreds of fragility functions, a simple metric is used to quantify the error from any single regenerated function with the deterministic one. Root mean square error (RMSE) is used to compare any two fragility functions. The results are further labeled qualitatively for any RMSE error range[3]: Match (<0.001), Excellent (0.001-0.005), Perfect (0.005-0.01), Very good (0.01-0.03), Good (0.03-0.06), Acceptable (0.06-0.1), Average (0.1-0.15), Poor (0.15-0.2), Bad (0.2-0.3), Very bad (>0.3).

Fig. 11 illustrates three-layer (i, $i+1$, and $i+2$) combinations at different LS values for the DiP parent model. Each line represents a combination passing through three different layers and ends at a specific RMSE error. For three-layer combinations, a total of $\binom{9}{3} = 84$ combinations are shown. As observed, increasing the LS value reduces the quality of regenerated functions. As a general trend, having SIL = 9 among the combinations leads to better predictions. Moreover, having three well-separated seismic intensity levels improves the prediction.

[3] Note: the emphasis is on the specific error ranges rather than the descriptive labels themselves.

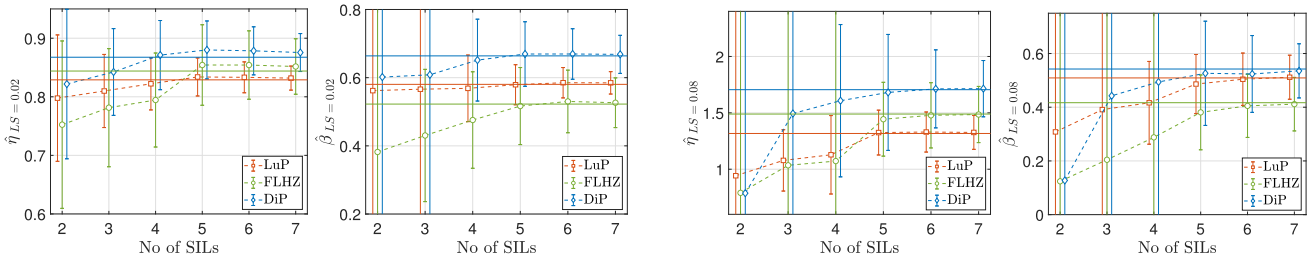

(a) LS = 0.02 (b) LS = 0.08

Fig. 10. Sensitivity of median and standard deviation of fragility functions regenerated with limited number of SILs. Results are based on GM uncertainty scenario and MLE. Bar plots present the mean and standard deviation of quantities. The horizontal solid line is the unbiased quantity calculated from deterministic model.

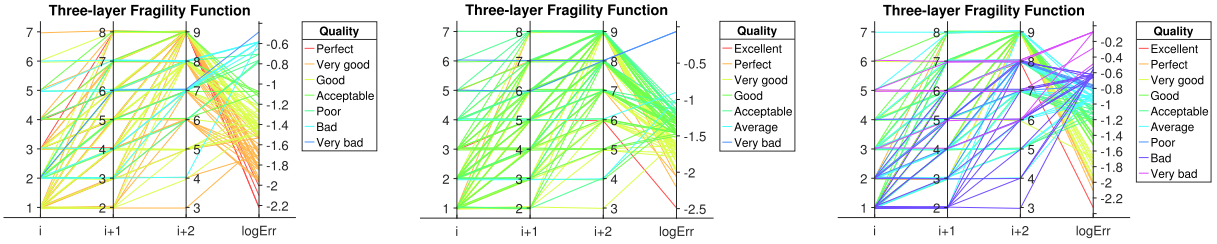

(a) LS = 0.01 (b) LS = 0.02 (c) LS = 0.04

Fig. 11. Quality of different three-layer combinational SILs to regenerate fragility functions. Results are based on GM uncertainty scenario, and MLE for DiP model with different LSs.

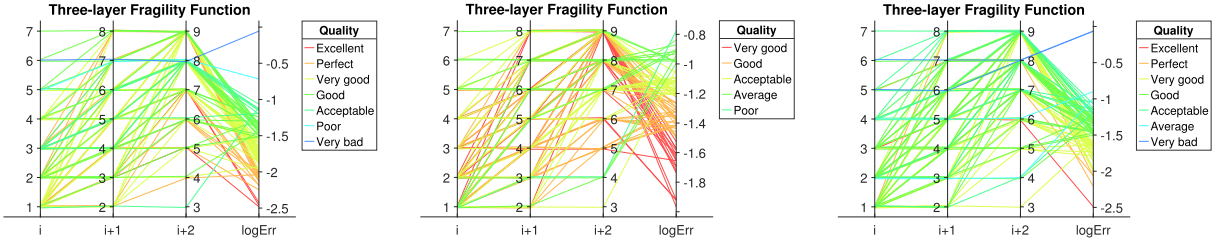

(a) LuP (b) FLHZ (c) DiP (Note: identical to 11(b))

Fig. 12. Quality of different three-layer combinational SILs to regenerate fragility functions. Results are based on GM uncertainty scenario and MLE for LS = 0.02 and different parent models.

Furthermore, Fig. 12 compares different parent models with the same LS value of 0.02. By observation, the quality of the regenerated fragility functions depends on the parent model and, more specifically, on the raw EDPs. Again, having SIL = 9 as one of three random layers significantly improves the quality.

4.4. Variance-Bias decomposition approach

The variance–bias decomposition approach combines the contributions of multiple uncertainty sources (ground motion RTR variability, material randomness, and modeling uncertainty) by separating variability that occurs within a given modeling approach from variability that arises between distinct modeling approaches. Two terms are therefore defined:

(1) *Intra-model (within-model) variability:* the dispersion of response and/or estimated fragility within a fixed parent model, driven primarily by RTR variability (e.g., under MSA/IDA) and, when considered, by additional material/modeling random variables introduced within that same parent model.

(2) *Inter-model (between-model) variability:* the dispersion attributable to differences among parent models (i.e., fundamentally different modeling strategies). In this framework, the inter-model term captures the spread of systematic model-to-model differences and can be interpreted as a distribution of model bias relative to one another (or relative to an external reference when available).

As shown in Fig. 3, a single curve represents intra-model variability (i.e., variance), while comparing any two curves highlights inter-model variability (i.e., bias). Now, the question is how to treat these variance-bias terms. [87] discuss two solutions that will be presented in this section.

4.4.1. Variance–variance assumption

The first perspective is based on variance-variance assumption. Typically in the PBEE framework, both variability sources are treated as only variance, leading to the so-called first-order assumption [88]. As a result, the following practical formulation can be used to combine the total variability:

$$\beta^2_{tot} = \beta^2_{intra} + \beta^2_{inter} \tag{10}$$

$$\beta^2_{intra} = \frac{1}{N_{\text{ff}}} \sum_{k=1}^{N_{\text{ff}}} \beta^2_{k,intra} \tag{11}$$

$$\beta^2_{inter} = \frac{1}{N_{\text{ff}} - 1} \sum_{k=1}^{N_{\text{ff}}} \left(\ln \overline{\eta} - \ln \eta_k \right)^2 \tag{12}$$

where η_k is the median of the quantity of interest (i.e., EDP given the IM or IM given EDP) for model k; and $\overline{\eta}$ is the mean of all η_k values.

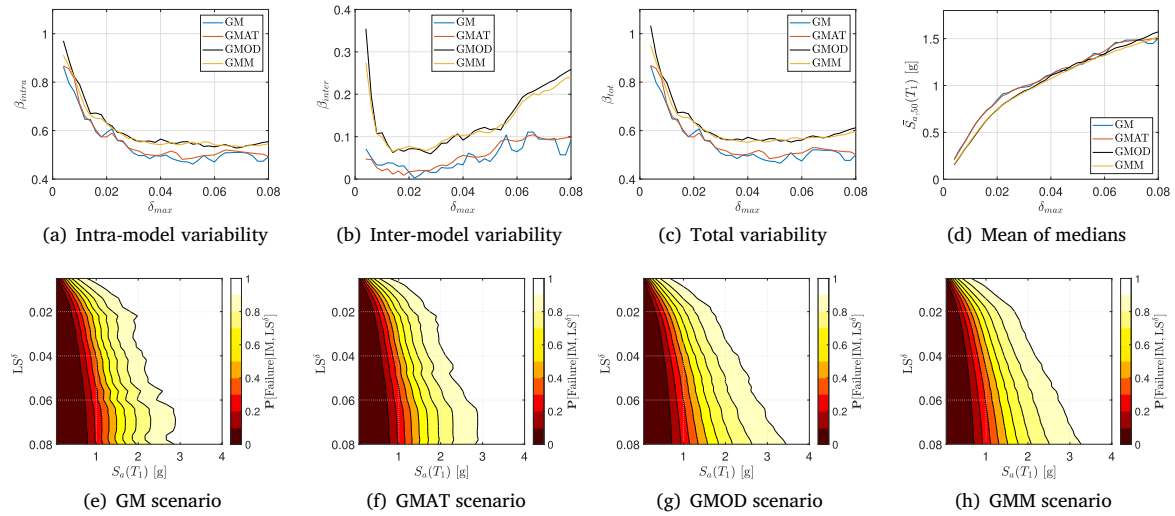

(a) Intra-model variability (b) Inter-model variability (c) Total variability (d) Mean of medians

(e) GM scenario (f) GMAT scenario (g) GMOD scenario (h) GMM scenario

Fig. 13. Unification of fragility functions for each of four uncertainty scenarios assuming first-order combination of variance and bias terms.

Fig. 13 illustrates the application of this approach to all four uncertainty scenarios. The intra- and inter-model variations are shown in Fig. 13(a) and 13(b), respectively. All four uncertainty scenarios exhibit a similar trend. The β_{intra} values decrease by increasing the limit state value and reach a stability of about 0.5 for GM and GMAT scenarios, and 0.55 for GMOD and GMM scenarios. Indeed, β_{intra} is a uniform average of dispersion from three parent models. On the other hand, β_{inter} has an average value of 0.05 for GM and GMAT scenarios, and 0.15 for GMOD and GMM scenarios. Its value decreases by the limit state, and then increases again. Overall, β_{inter} is much smaller than β_{intra}, and thus, the value of β_{tot} is close to intra-model variability. See Fig. 13(c). Fig. 13(d) illustrates the variation of $\overline{\eta}$ (in our example $\overline{S}_{a,50}(T_1)$). As seen, the mean of median curves from different scenarios are very close. Finally, Fig. 13(e) to 13(h) present the 3D fragility functions obtained from mean of median values and total dispersion for each of four uncertainty scenarios.

4.4.2. Variance–bias assumption

In the second perspective, bias is handled separately from variance. Therefore, a bias correction factor should be computed that requires information about the baseline "accurate" model (which is by itself a difficult choice). The bias can be simply computed as:

$$\text{bias}_i = \frac{\eta_i}{\eta_{baseline}} - 1 \xrightarrow[\text{fragility function}]{\text{EDP-based}} \text{bias}_i = \frac{S^i_{a,50}(T_1)|\text{LS}^j}{S^{\text{baseline}}_{a,50}(T_1)|\text{LS}^j} - 1 \qquad (13)$$

where i refers to parent model, and j presents the limit state value.

In its most ideal form, one may need to have access to the results of probabilistic experimental (e.g., shake table) tests using the same ground motion records that are used in numerical simulation (e.g., MSA). Such an effort requires hundreds of shake table tests and is practically impossible to achieve. To the best of the authors' knowledge, [89] fulfilled the first-ever probabilistic IDA test with a very simple SDOF model (a pin-connected boxlike structure with a dog-bone member providing lateral stiffness). A total of 12 random specimens were subjected to 7 ground motion records at 4 intensity levels. Such extensive experimental results provide an excellent basis to validate the numerical models and determine the potential bias due to modeling assumptions and/or material randomness. In the absence of such results, one may consider the following three alternatives, each of which comes with assumptions and limitations.

Bias Estimation (I)

For a model without any field or experimental test, the only option is to assume one of the parent models as the baseline model. Such a choice depends on the confidence of the modeler in the selected numerical technique and the overall capability of that technique in predicting seismic response (as typically reported in the literature). In this report, the FLHZ is assumed to be the baseline model, which is technically an intermediate model between distributed plasticity and concentrated plasticity models. Fig. 14(a) illustrates the computed bias for two other models. The resulted bias from GM and GMAT scenarios fluctuates around the baseline. Overall, the bias from GMOD and GMM scenarios for DiP is always positive, while the LuP creates a slightly negative bias.

Bias Estimation (II)

The second approach roots in the availability of limited (and not probabilistic) experimental tests. In these methods, it is assumed the structural system is analyzed under multiple ground motion records with different seismic intensities. Also, it is assumed that the computed bias between the limited experimental test and the numerical model is expandable to the entire probabilistic numerical simulations. The procedure is summarized in a pseudo-algorithm 2. This approach is implemented on three parent models used in this report.

Experimental support and $R_{E/N} - S_a(T_1)$ mapping. The 2010 UCSD blind prediction contest includes the outcome of shake table test on a single RC bridge column using six ground motions. The recorded fundamental periods, critical damping ratio, first-mode spectral acceleration, drift and base shear time histories are available [81]. For the sake of approach (II), three parent models (i.e., DiP, FLHZ, and LuP) are validated with experimental results in terms of drift ratio. For each ground motion, first a baseline correction is implemented, and then, the maximum absolute response from experimental test and numerical model is reported as EDP_{exp} and EDP_{num}, respectively. These quantities are later used in Algorithm 2 to compute the $R_{E/N}$. The computed $R_{E/N}$ is next paired with $S_a(T_1)$ to form one point in $R_{E/N} - S_a(T_1)$ space. This procedure is repeated for all six ground motions. Then, a 1st order polynomial curve is fitted into discrete data points which covers the $S_a(T_1)$ range from 0.2–1.0 g. One may note that the probabilistic structural simulations (i.e., MSA in this report) covers $S_a(T_1)$ range from 0.25–0.95 g (which is within the fitted line). This procedure is repeated for two other parent models too (FLHZ, and LuP). Fig. 15(a) illustrates the resulting $R_{E/N} - S_a(T_1)$ relationship which is mapped into three parent models. The $R_{E/N}$ is mapped into row (initial) MSA results. At each stripe, the values of all row EDPs are multiplied by associated $R_{E/N}$ value. The resulted EDP* values are used generate fragility functions. These functions are treated as baseline models, and are used to compute the bias using Eq. (13).

The variation of bias for various models and uncertainty scenarios is shown in Fig. 14(b) using the second approach. As seen, there is a

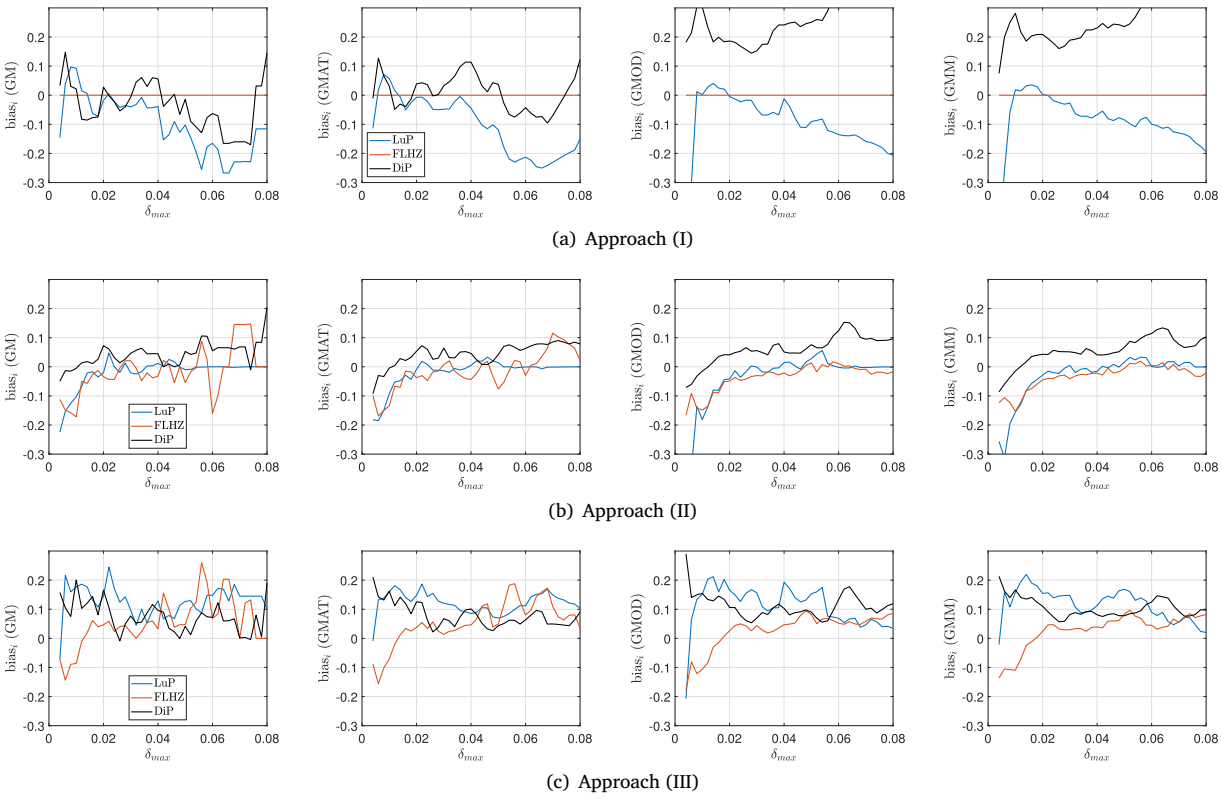

(a) Approach (I)

(b) Approach (II)

(c) Approach (III)

Fig. 14. Bias estimation in the results of probabilistic structural analyses using three approaches.

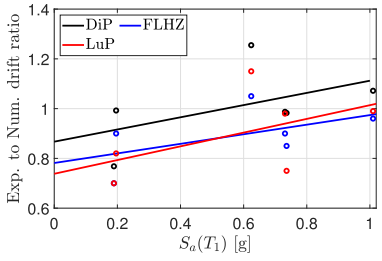

(a) $R_{E/N} - S_a(T_1)$ relations from analyst's best model validation

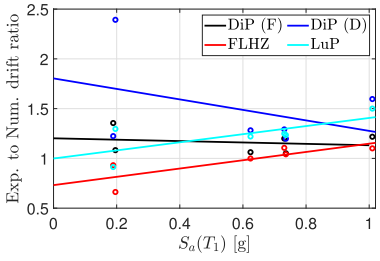

(b) $R_{E/N} - S_a(T_1)$ relations from blind prediction contest's results

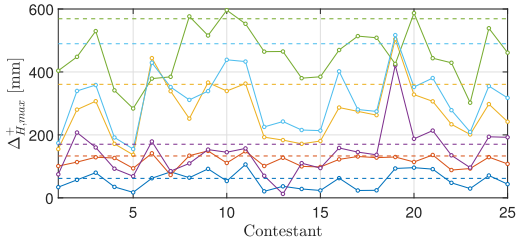

(c) Maximum displacement from contestants in positive direction

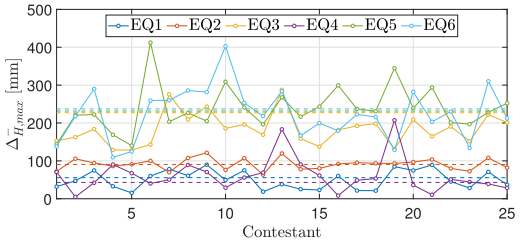

(d) Maximum displacement from contestants in negative direction

Fig. 15. Comparison of results from shake table test and numerical simulations for the case study bridge column.

considerable improvement in bias estimation. For the majority of $\delta_{\max}$ limit states, the bias is limited to ±10%.

Bias Estimation (III)

Approach (II) determines the $R_{E/N} - S_a(T_1)$ relationship based on the same parent model which is used later by the analyst to perform the probabilistic simulations. Therefore, all the modeling assumptions by the analyst (correct or incorrect) are buried in the process. One solution to overcome this shortcoming is to use an independent numerical simulation to determine the $R_{E/N} - S_a(T_1)$ relationship. The third bias estimation approach is similar to the second one in the sense that both use the results of experimental tests to estimate the bias in numerical models. In this approach, the outcome of carefully-processed blind pre-

Algorithm 2 Bias estimation (II) using validated numerical simulations with experimental tests

Inputs: EDP from experimental test, and the corresponding numerical results. Results from probabilistic numerical simulation.
Output: Bias factor for each of parent models.

procedure BIAS CALCULATION
  Develop a total of N_{PRT} parent models. ▷ In this paper: LuP, FLHZ, DiP
  for $i = 1, \ldots, N_{\text{PRT}}$ **do**
    for $j = 1, \ldots, N_{\text{RCD}}$ **do** ▷ N_{RCD}: number of limited ground motion records.
      $R^{i,j}_{E/N} = \frac{\text{EDP}_{\text{exp}}}{\text{EDP}_{num}}$
      Determine the effective intensity measure value, IM^j
    end for
    Collect all pairs of $R^{i,j}_{E/N} - \text{IM}^j$.
    ft = `fittype` ('`poly1`'); ▷ Define fit type. `poly1` and `poly2`: 1st and 2nd order polynomial
    [Fit(i).bias, ~] = `fit` (IM, $R^i_{E/N}$, ft) ▷ Fit a function of discrete data points.
    Map the IM-dependent bias, Fit(i).bias, into the row results from probabilistic numerical simulation, e.g., MSA.
    for $k = 1, \ldots, N_{\text{IM}}$ **do**
      EDP^*_k = Fit(i).bias (k) × EDP_k ▷ Fit(i).bias (k): scale factor at level k.
    end for
    Fit an analytical fragility function and determine $\eta_{baseline}$. ▷ See Eq. 3
    Calculate bias using Eq. (13). ▷ Numerator is η from original EDPs.
  end for
end procedure

diction contest is used to estimate the $R_{E/N} - S_a(T_1)$ relationship. The process is essentially similar to that explained in Algorithm 2. However, instead of calculating ${R_{E/N}}^{i,j}$ using one EDP*num*, the median of all numerical models (collected from participants in the blind prediction), EDPnum^{median} is used.

Contest-based dataset. For approach (III), the results of 25 contestants are used. The first 13 results belong to force-based fiber model, DiP (F), followed by 4 results based on displacement-based fiber model, DiP (D), 3 results based on FLHZ, and finally 5 results for LuP model. The results of numerical simulations for all contestants are shown in Figs. 15(c) and 15(d) (solid lines), while the horizontal dashed line presents the shake table results. For each of these parent models, the median of maximum absolute EDP is compared to the experimental results. The results of $R_{E/N} - S_a(T_1)$ relationship is shown in Fig. 15(b).

A sample of such a $R_{E/N} - S_a(T_1)$ relationship is shown in Fig. 14(c) using the results of 25 participants in the 2010 UCSD Blind Prediction Contest. The variation of bias for various models and uncertainty scenarios is shown in Fig. 14(c) using the third approach. Similar to approach (II), there is an improvement in bias estimation (compared to approach (I)); however, the trend is different from approach (II). It seems that the bias curves fluctuate around $bias = 0.1$ instead of the zero line. This clearly roots in the variation of $R_{E/N} - S_a(T_1)$ relationship.

5. Conclusions

This paper has embarked on an extensive exploration of seismic fragility functions, presenting a comprehensive examination of various methodologies and critical considerations. The findings highlight the significance of selecting appropriate seismic intensity measures and their distributions, underlining how these choices fundamentally influence the derived fragility functions.

The core contributions of this work are twofold: first, it introduces seismic fragility functions that integrate both modeling and material uncertainty sources within probabilistic simulations. Second, it proposes a series of approaches for combining fragility functions derived from differing modeling strategies or for developing multi-fidelity fragility models that incorporate multiple modeling assumptions.

We have discussed four distinct methodologies. The decision tree method, which employs a weighted scheme to combine different fragility functions, is praised for its simplicity and flexibility, offering various schemes from basic weighting to decision criteria and user-defined weights. Conversely, the nonuniform weight function approach merges fragility functions using intensity measure-dependent weights, proving especially beneficial when the accuracy of modeling strategies varies with the loading protocol or when the analyst possesses greater confidence in specific parts of the simulation.

The mixed-EDP method integrates diverse model fidelities with raw results to craft a unified surrogate model, subsequently utilized to develop a comprehensive fragility function. This approach is particularly valuable in regions with scant data, facilitating the combination of structural models of varying fidelity by assigning weights based on the user's judgment and confidence in each model strategy across different IM regions. Adjusting these weights allows the mixed probabilistic seismic demand model to encapsulate the responses of individual source models and their combinations, showcasing its utility in complex models where each response history analysis is costly, emphasizing the criticality of leveraging every available point estimate.

The interplay between intra-model and inter-model variability, elucidated through the variance-variance and variance-bias methods, shows the uncertainties inherent in seismic risk assessments. We have outlined three methods for computing bias terms, i.e., the analyst's belief and confidence in the model; leveraging limited experimental test results; and referencing established relations from literature or benchmark workshops. These methods necessitate a robust understanding of the problem's physics or access to reliable sources for bias term computation.

Ultimately, this paper positions itself as a valuable resource for researchers, engineers, and practitioners engaged in seismic risk assessment. By combining existing knowledge and advancing the discourse on contemporary challenges and innovative methodologies, it aims to propel the domain of seismic risk analysis forward, fostering enhanced understanding and application of seismic fragility functions in the pursuit of more resilient structures.

Disclaimer

Certain commercial equipment, instruments, or materials are identified in this paper to foster understanding. Such identification does not imply recommendation or endorsement by the National Institute of Standards and Technology (NIST), nor does it imply that the materials or equipment identified are necessarily the best available for the purpose.

CRediT authorship contribution statement

Mohammad Amin Hariri-Ardebili: Writing – review & editing, Writing – original draft, Visualization, Validation, Supervision, Software, Resources, Methodology, Investigation, Formal analysis, Data curation, Conceptualization; **Siamak Sattar:** Writing – review & editing, Validation, Investigation, Conceptualization.

Data availability

Data will be made available on request.

Declaration of competing interest

The authors declare that they have no known competing financial interests or personal relationships that could have appeared to influence the work reported in this paper.

Acknowledgement

This work was supported by the National Institute of Standards and Technology (NIST), USA. Dr. Amin Hariri was supported through PREP, USA agreement no. 70NANB23H024 between NIST and the University of Maryland, College Park.

The authors would like to thank the reviewers for their constructive comments, which have greatly contributed to improving the final version of this paper.

Appendix A. Acronyms

C	Collapse
CDF	Cumulative distribution function
DiP	Distributed plasticity
DOE	Design of experiment
DS	Damage State
EDP	Engineering demand parameter
FLHZ	Finite-length hinge zone
GM	Ground motion RTR variability only
GMAT	Ground motion RTR variability and material uncertainty
GMOD	Ground motion RTR variability and modeling uncertainty
GMM	Ground motion RTR variability, material and modeling uncertainty
IDA	Incremental dynamic analysis
IM	Intensity measure
LHS	Latin hypercube sampling
LS	Limit state
LuP	Lumped plasticity
MCS	Monte Carlo Simulation
MLE	Maximum likelihood estimation
MSA	Multiple stripes analysis
PEER	Pacific Earthquake Engineering Research
PBEE	Performance-based earthquake engineering
PDF	Probability distribution function
PGA	Peak Ground Acceleration
RC	Reinforced concrete
RMSE	Root mean square error
RTR	Record-to-record
SDOF	single degree of freedom
SIL	Seismic intensity level
WS	Weighting scheme

References

[1] Silva V, Bazzurro P, Vamvatsikos D. Preface to the special issue: the evolution of fragility and vulnerability. the origin story of a preface. Bull Earthq Eng 2021;19:6269–70.
[2] Kennedy RP, Cornell CA, Campbell RD, Kaplan S, Perla HF. Probabilistic seismic safety study of an existing nuclear power plant. Nucl Eng Des 1980;59:315–38.
[3] Cornell CA, Krawinkler H. Progress and challenges in seismic performance assessment. http://peer.berkeley.edu/news/2000spring/index.html; 2000.
[4] Mackie KR, Stojadinovic B. Fragility basis for California highway overpass bridge seismic decision making. Pacific Earthquake Engineering Research Center, College of Engineering, University of California, Berkeley; 2005.
[5] Shinozuka M, Feng MQ, Lee J, Naganuma T. Statistical analysis of fragility curves. J Eng Mech 2000;126:1224–31.
[6] Lupoi G, Franchin P, Lupoi A, Pinto PE. Seismic fragility analysis of structural systems. J Eng Mech 2006;132(4):385–95.
[7] Kafali C, Grigoriu M. Seismic fragility analysis: application to simple linear and nonlinear systems. Earthq Eng Struct Dyn 2007;36(13):1885–900.
[8] Jalayer F, De Risi R, Manfredi G. Bayesian cloud analysis: efficient structural fragility assessment using linear regression. Bull Earthq Eng 2015;13(4):1183–1203.
[9] Baker JW. Efficient analytical fragility function fitting using dynamic structural analysis. Earthq Spectra 2015;31(1):579–99.
[10] Noh HY, Lallemant D, Kiremidjian AS. Development of empirical and analytical fragility functions using kernel smoothing methods. Earthq Eng Struct Dyn 2015;44(8):1163–80.
[11] Ghosh S, Chakraborty S. Seismic fragility analysis of structures based on Bayesian linear regression demand models. Probab Eng Mech 2020;61:103081.
[12] Altieri D, Patelli E. An efficient approach for computing analytical non-parametric fragility curves. Struct Saf 2020;85:101956.
[13] Porter KA, Kennedy R, Bachman R. Creating fragility functions for performance-based earthquake engineering. Earthq Spectra 2007;23:471–89.
[14] Colangelo F. On the computation of seismic fragility curves. In: 14th World conference on earthquake engineering. 2008,.
[15] Straub D, Der Kiureghian A. Improved seismic fragility modeling from empirical data. Struct Saf 2008;30(4):320–36.
[16] Lallemant D, Kiremidjian AS, Burton H. Statistical procedures for developing earthquake damage fragility curves. Earthquake Eng Struct Dyn 2015;44:1373–89.
[17] Mai C, Konakli K, Sudret B. Seismic fragility curves for structures using non-parametric representations. Front Struct Civ Eng 2017;11(2):169–86.
[18] Iervolino I. Assessing uncertainty in estimation of seismic response for PBEE. Earthq Eng Struct Dyn 2017;46(10):1711–23.
[19] Zentner I. A general framework for the estimation of analytical fragility functions based on multivariate probability distributions. Struct Saf 2017;64:54–61.
[20] Cutfield MR, Ma Q TM. Solution strategies for three problems in empirical fragility curve derivation using the maximum likelihood method. J Earthq Eng 2018;22(3):435–53.
[21] Long XH, Xie ZY, Fan J, Miao Y. Convex model-based calculation of robust seismic fragility curves of isolated continuous girder bridge. Bull Earthq Eng 2018;16:155–82.
[22] Andriotis CP, Papakonstantinou KG. Extended and generalized fragility functions. J Eng Mech 2018;144(9):04018087.
[23] Xu J, Liao L, Zhang Y, Wang D. Efficient seismic fragility analysis of structures from dynamic reliability perspective. Eng Struct 2022;271:114889.
[24] Hariri-Ardebili MA, Sattar S. Uncertainty and bias in fragility estimates by intensifying artificial accelerations. Probab Eng Mech 2023;74:103545.
[25] Muntasir Billah A, Shahria Alam M. Seismic fragility assessment of highway bridges: a state-of-the-art review. Struct Infrastruct Eng 2015;11(6):804–32.
[26] Hariri-Ardebili MA, Saouma VE. Seismic fragility analysis of concrete dams: a state-of-the-art review. Eng Struct 2016;128:374–99.
[27] Rajkumari S, Thakkar K, Goyal H. Fragility analysis of structures subjected to seismic excitation: a state-of-the-art review. Structures 2022;40:303–16.
[28] Kaynia AM, Taucer F, Hancilar U. Guidelines for deriving seismic fragility functions of elements at risk: buildings, lifelines, transportation networks and critical facilities. Publications Office; 2013.
[29] Pitilakis K, Crowley H, Kaynia A. SYNER-G: typology definition and fragility functions for physical elements at seismic risk. Geotech Geol Earthq Eng 2014;27.
[30] The World Bank Group. Fragility and vulnerability assessment guide. THE GLOBAL LIBRARY OF SCHOOL INFRASTRUCTURE; 2019.
[31] Beer M, Kougioumtzoglou IA, Patelli E, Au S-K. Encyclopedia of earthquake engineering. Springer Heidelberg; 2015.
[32] Nazri FM. Seismic fragility assessment for buildings due to earthquake excitation. Springer; 2018.
[33] Porter KA. A Beginner's guide to fragility, vulnerability, and risk. https://www.sparisk.com/pubs/Porter-beginners-guide.pdf; 2021. Last viewed March 2022.
[34] Lyu M-Z, Feng D-C, Cao X-Y, Beer M. A full-probabilistic cloud analysis for structural seismic fragility via decoupled m-PDEM. Earthq Eng Struct Dyn 2024;53(5):1863–81.
[35] Mehdipour R, Hamidia M, Asjodi AH, Dolatshahi KM. Seismic safety assessment of reinforced concrete columns through multi-variate fragility analysis. Reliab Eng Syst Saf 2025;111809.
[36] Lyu M-Z, Fei Z-J, Feng D-C. Vine-copula-based multi-dimensional fragility analysis of nuclear power plant under sequential earthquakes. Struct Saf 2024;110:102494.
[37] Yan Y, Xia Y, Sun L. Hierarchical and mixed uncertainty quantification for simulation-based structural seismic fragility analysis. Eng Struct 2024;316:118579.
[38] Misra S, Bocchini P. MetaIMNet: a physics-informed neural network architecture for surrogate response and fragility modeling of structures subjected to time-varying hazard loads. Struct Saf 2025;118:102650.
[39] Zheng Z, Zhang P, Pan X, Yang F. Deep learning-enhanced multi-fidelity framework for seismic fragility analysis of nuclear power plant containment structures. Reliab Eng Syst Saf 2025;266:111884.
[40] Ma X, Xiong W, Zhou D, Cai CS. Fragility analysis of multiple bridges under scour conditions enabled by knowledge transferred from single bridge. Reliab Eng Syst Saf 2025;111837.
[41] Xing L, Gardoni P, Zhou Y, Zhang P. DNN-metamodeling and fragility estimate of high-rise buildings with outrigger systems subject to seismic loads. Reliab Eng Syst Saf 2025;253:110572.
[42] Yan Y, Xie Y, Xia Y, Sun L. Systematic investigation on surrogate and active learning-based multivariate seismic fragility analysis under multiple sources of uncertainties. Reliab Eng Syst Saf 2025;265:111588.
[43] Thedy J, Liao K-W. Machine learning-enhanced fragility curves: advancing reliability and safety of structures in seismic risk assessment. Reliab Eng Syst Saf 2025;264:111361.

[44] de Almeida Torres Filho RJ, Segura RL, Paultre P. Comparative analysis of regression techniques for dual-fidelity surrogates in concrete gravity dams. Reliab Eng Syst Saf 2025;111509.
[45] Jin S, Xu S, Shen T, Wang H, Cao X, Jia H. Time-dependent fragility analysis and risk assessment of nuclear containment structure subjected to internal pressure considering chloride-induced corrosion of reinforcing steel. Reliab Eng Syst Saf 2025;266:111736.
[46] Nardin C, Marelli S, Bursi OS, Sudret B, Broccardo M. UQ state-dependent framework for seismic fragility assessment of industrial components. Reliab Eng Syst Saf 2025;111067.
[47] Gauchy C, Feau C, Garnier J. Uncertainty quantification and global sensitivity analysis of seismic fragility curves using kriging. Int J Uncertain Quantif 2024;14(4):39–63.
[48] Kim J, Kim T. Efficient seismic fragility analysis considering uncertainties in structural systems and ground motions. Earthq Eng Struct Dyn 2025;54(1):206–26.
[49] Lee D, Wang Z, Song J. Efficient seismic reliability and fragility analysis of lifeline networks using subset simulation. Reliab Eng Syst Saf 2025;260:110947.
[50] Monti G, Rabi RR, Demartino C. Spectrum-consistent ag-based fragility curves. Reliab Eng Syst Saf 2024;245:109977.
[51] Wang J, Gao S, Yu L, Zhang D, Xie C, Chen K, et al. Data-driven lightning-related failure risk prediction of overhead contact lines based on Bayesian network with spatiotemporal fragility model. Reliab Eng Syst Saf 2023;231:109016.
[52] Xie Y. Impact of component damage correlations on seismic fragility and risk assessment of multi-component bridge systems. Struct Saf 2025;102635.
[53] Bradley B. Epistemic uncertainties in component fragility functions. Earthq Spectra 2010;26(1):41–62.
[54] Baraschino R, Baltzopoulos G, Iervolino I. R2r-EU: software for fragility fitting and evaluation of estimation uncertainty in seismic risk analysis. Soil Dyn Earthq Eng 2020;132:106093.
[55] Grigoriu M, Radu A. Are seismic fragility curves fragile? Probab Eng Mech 2021;63:103115.
[56] Iervolino I. Estimation uncertainty for some common seismic fragility curve fitting methods. Soil Dyn Earthquake Eng 2022;152:107068.
[57] Ayyub BM, Chao RU. Uncertainty modeling in civil engineering with structural and reliability applications. Uncertain Model Anal Civ Eng 1997;1–8.
[58] Bakalis K, Vamvatsikos D. Seismic fragility functions via nonlinear response history analysis. J Struct Eng 2018;144(10):04018181.
[59] Padgett JE, Nielson BG, DesRoches R. Selection of optimal intensity measures in probabilistic seismic demand models of highway bridge portfolios. Earthquake Eng Struct Dyn 2008;37:711–25.
[60] Giannini R, Paolacci F, Phan HN, Corritore D, Quinci G. A novel framework for seismic risk assessment of structures. Earthq Eng Struct Dyn 2022;51(14):3416–33.
[61] Hariri-Ardebili MA, Sattar S. Uncertainty and bias in generic ground motion sets used for PBEE. Structures 2023;57.
[62] Vamvatsikos D, Dolšek M. Equivalent constant rates for performance-based seismic assessment of ageing structures. Struct Saf 2011;33(1):8–18.
[63] Dolšek M. Incremental dynamic analysis with consideration of modeling uncertainties. Earthq Eng Struct Dyn 2009;38:805–25.
[64] Celarec D, Dolšek M. The impact of modelling uncertainties on the seismic performance assessment of reinforced concrete frame buildings. Eng Struct 2013;52:340–54.
[65] Vamvatsikos D, Cornell CA. Incremental dynamic analysis. Earthq Eng Struct Dyn 2002;31:491–514.
[66] Jalayer F, Cornell CA. Alternative non-linear demand estimation methods for probability-based seismic assessments. Earthquake Eng Struct Dyn 2009;38:951–72.
[67] Miano A, Jalayer F, Ebrahimian H, Prota A. Cloud to IDA: efficient fragility assessment with limited scaling. Earthq Eng Struct Dyn 2018;47(5):1124–47.
[68] Celik OC, Ellingwood BR. Seismic fragilities for non-ductile reinforced concrete frames–role of aleatoric and epistemic uncertainties. Struct Saf 2010;32:1–12.
[69] Elnashai AS, Chryssanthopoulos M. Effect of random material variability on seismic design parameters of steel frames. Earthq Eng Struct Dyn 1991;20(2):101–14.
[70] Lee T-H, Mosalam KM. Seismic demand sensitivity of reinforced concrete shear-wall building using FOSM method. Earthq Eng Struct Dyn 2005;34(14):1719–36.
[71] Hariri-Ardebili MA, Segura Jr CL, Sattar S. Modeling and material uncertainty quantification of RC structural components. Struct Saf 2024;106:102401.
[72] Haselton CB, Goulet CA, Mitrani-Reiser J, Beck JL, Deierlein GG, Porter KA, et al. An assessment to benchmark the seismic performance of a code-conforming reinforced concrete moment-frame building, PEER report 2007/12. Tech. Rep.; Pacific Earthquake Engineering Research Center, University of California; Berkeley, California; 2008.
[73] Sattar S, Liel AB, Martinelli P. Quantification of modeling uncertainties based on the blind prediction contest submissions. In: Structures congress 2013: bridging your passion with your profession. 2013, p. 1997–2008.
[74] Bradley B. A framework for validation of seismic response analyses using seismometer array recordings. Soil Dyn Earthq Eng 2011;31(3):512–20.
[75] Bradley B. A critical examination of seismic response uncertainty analysis in earthquake engineering. Earthq Eng Struct Dyn 2013;42(11):1717–29.
[76] Lee TH, Mosalam KM. Probabilistic seismic evaluation of reinforced concrete structural components and systems. Tech. Rep. 2006/04; Pacific Earthquake Engineering Research Center; 2006.
[77] Haselton CB, Deierlein GG. Assessing seismic collapse safety of modern reinforced concrete moment frame buildings, report no 2007/08. Tech. Rep. TR 156, ; John A. Blume Earthquake Engineering Center Department of Civil Engineering; 2006.
[78] Aslani H, Miranda E. Probabilistic earthquake loss estimation and loss disaggregation in buildings. Ph.D. thesis; Stanford University, Stanford; Palo-Alto, CA; 2005.
[79] Hariri-Ardebili MA. Quantifying modeling uncertainties in seismic analysis of dams: insights from an international benchmark study. Earthq Eng Struct Dyn 2024;53(3):1168–94.
[80] Bolzon G, Sterpi D, Mazzà G, Frigerio A. Numerical analysis of dams: proceedings of the 15th ICOLD international benchmark workshop; vol. 91. Springer Nature; 2020.
[81] Terzic V, Schoettler MJ, Restrepo JI, Mahin SA. Concrete column blind prediction contest 2010: outcomes and observations, PEER report no. 2015/01. Tech. Rep.; Pacifi c Earthquake Engineering Research Center; California, Berkeley; 2015.
[82] Segura Jr CL, Sattar S, Hariri-Ardebili MA. Quantifying material uncertainty in seismic evaluations of reinforced concrete bridge column structures. ACI Struct J 2022;119(3):141–52.
[83] Rossetto T, D'Ayala D, Ioannou I, Meslem A. Evaluation of existing fragility curves. In: SYNER-G: typology definition and fragility functions for physical elements at seismic risk. Springer; 2014, p. 47–93.
[84] Ning C-L, Feng D-C. Probabilistic indicator to classify the failure mode of reinforced-concrete columns. Mag Concr Res 2019;71(14):734–48.
[85] Chatzidaki A, Vamvatsikos D. Mixed probabilistic seismic demand models for fragility assessment. Bull Earthq Eng 2021;19(15):6397–421.
[86] Feller W. An introduction to probability theory and its applications, vol 2. John Wiley & Sons; 2008.
[87] Lachanas CG, Vamvatsikos D. Model type effects on the estimated seismic response of a 20-story steel moment resisting frame. J Struct Eng 2021;147(6):04021078.
[88] Cornell CA, Jalayer F, Hamburger RO, Foutch DA. Probabilistic basis for 2000 SAC federal emergency management agency steel moment frame guidelines. J Struct Eng 2002;128(4):526–33.
[89] Deng P, Pei S, van de Lindt JW, Zhang C. Experimental investigation of seismic uncertainty propagation through shake table tests. J Struct Eng 2018;144(3):06017009.
[90] A Der Kiureghian, O Ditlevsen, Aleatory or epistemic? Does it matter?, Struct Saf 2009;31:105–12.